

Figure 1. Overview of the AWA beamline showing only components relevant to the present experiment (a) with simulated emittance evolution in the skew-quadrupole channel (b), and associated beam (c) and phase-space (d) distributions simulated at X1 and X2. In (a) the labels “SQ*i*” and “X*j*” respectively correspond to skew-quadrupole magnets and insertable scintillating screens. The diagnostics station located at X2 also comprises scanning slits for emittance measurements. In (d) the phase-space simulated at X1 is cylindrical-symmetric so that only  $(x, x')$  distribution (blue) is reported while both  $(x, x')$  (red) and  $(y, y')$  are reported at X2. In (b) we introduce the uncorrelated emittance as  $\varepsilon_u \equiv \sqrt{\varepsilon_{4d}}$  for convenience.

$(y, y')$ . In the most general case, the 4D emittance  $\varepsilon_{4d} \equiv [\det(\Sigma)]^{1/2}$  is conserved under linear forces. More generally, owing to its positive-definite nature,  $\Sigma$  can be diagonalized [15] via a symplectic transformation  $A$  as  $A\Sigma A^T = \text{diag}(\beta_+^* \varepsilon_+, \varepsilon_+ / \beta_+^*, \beta_-^* \varepsilon_-, \varepsilon_- / \beta_-^*)$  with  $\varepsilon_{\pm}$  being the eigenemittances and  $\beta_{\pm}^* > 0$  are the betatron functions [16]. Specifically, the quantity  $\sqrt{\beta_{\pm} \varepsilon_{\pm}} / \gamma$  (where  $\gamma$  is the Lorentz factor) represents the electron-beam rms size at a waist. The eigenemittances are degenerate solutions of the characteristic equation of  $\det(J_4 \Sigma - i \varepsilon_{\pm} I) = 0$ , where  $i \equiv \sqrt{-1}$ ,  $I$  is the  $4 \times 4$  identity matrix and  $J_4 \equiv \begin{bmatrix} J & 0 \\ 0 & J \end{bmatrix}$  with  $J \equiv \begin{bmatrix} 0 & 1 \\ -1 & 0 \end{bmatrix}$ . They are related to the projected emittances via [17]

$$\varepsilon_{\pm} = \frac{1}{2} [\xi_{\pm}^{1/2} \pm \xi_{\mp}^{1/2}], \quad (2)$$

where  $\xi_{\pm} \equiv \varepsilon_x^2 + \varepsilon_y^2 + 2 \det(\langle \mathbf{X} \mathbf{Y}^T \rangle) \pm 2 \varepsilon_{4d}$ . Equation 2 gives a prescription to tailor the initial cross-plane correlation with given eigenemittance computed within the 4-D phase space distribution to ultimately – after decoupling of the beam dynamics – control the transverse projected emittance partition [18]. Such a ca-

pability is foreseen to have applications in the design of future high-energy particle accelerators [9] and free-electron lasers [11].

The emittance-transfer experiment was performed at the Argonne Wakefield Accelerator (AWA) diagrammed in Fig.1(a) [19]. The beamline consists of a radiofrequency (RF) photoinjector comprising a Caesium-Telluride ( $\text{Cs}_2\text{Te}$ ) photocathode mounted in a  $1 + \frac{1}{2}$  resonant cavity (the RF gun). In our experiment,  $\sim 1$ -nC electron bunches were emitted from the gun into a linear accelerator (linac) that boosts the beam energy to  $\sim 42$  MeV. To produce a beam in an initial coupled state, the photocathode was immersed in an axial magnetic field  $B_c \hat{\mathbf{z}}$  resulting in a particle emitted at position  $\mathbf{r}^T \equiv (x, y)$  on the photocathode to acquire an ab-initio angular momentum, arising from the non-vanishing angular components of the vector potential  $\mathbf{A} \simeq \frac{B_c}{2} (-y \hat{\mathbf{x}} + x \hat{\mathbf{y}})$ , given by  $\mathbf{L} = \mathbf{r} \times e \mathbf{A} = \frac{e B_c}{2} r^2 \hat{\mathbf{z}}$ . Correspondingly, the  $2 \times 2$  anti-diagonal blocks of the beam covariance matrix are given by  $\langle \mathbf{X} \mathbf{Y}^T \rangle = -\langle \mathbf{Y} \mathbf{X}^T \rangle = \mathcal{L} J$  where  $\mathcal{L} \equiv \frac{\langle L \rangle}{2 m c}$  is the beam magnetization, and the ensemble-averaged angular momentum is  $\langle L \rangle = e B_c \sigma_c^2$  where  $\sigma_c \equiv \sqrt{\langle x^2 \rangle} = \sqrt{\langle y^2 \rangle}$  is the transverse rms size of the axi-symmetric laser spot on the photocathode [20, 21]. The ultraviolet laser pulse used to trigger the emission was transversely shaped to ensure the distribution of the emitted beam is cylindrical-symmetric and homogeneous [22]; the measured laser transverse distribution on the virtual photocathode – a 1-to-1 optical image of the photocathode – appears in Fig. 2(a). Likewise, the full-width half-maximum of the laser-pulse du-

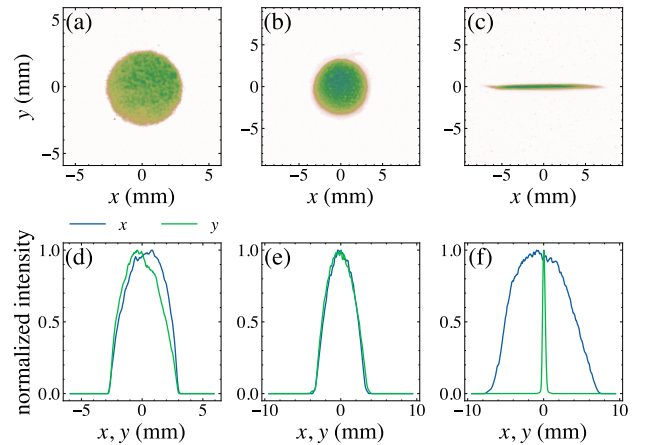


Figure 2. Representative measurements of the laser distribution on the virtual cathode (a), and transverse electron-beam distribution recorded at X1 for the coupled beam (b) and at X2 for the decoupled beam (c). The lower row displays the horizontal (blue) and vertical (green) projection computed from the upper row. The solenoid lens “LF” was set to produce  $B_c = 140$  mT and switching between coupled and uncoupled configuration is achieved by powering the skew quadrupole magnets (SQ1-3) to their nominal values.

ration was  $\sim 400$  fs to guarantee the evolution of the beam dynamics is dominated by the space-charge-driven expansion resulting in a quasi uniformly-charged ellipsoidal distribution with space-charge forces linearly dependent on the positions within the bunch [23, 24]. Such a “blow-out” regime mitigates emittance growth arising from nonlinear space-charge effects. Downstream of the linac, three skew-quadrupole magnets SQ1-3 is used to apply a torque to cancel the incoming beam’s angular momentum; see Fig. 1(b). In the process, the initially round beam is transformed into a flat beam with an asymmetric emittance partition [9, 21]; see Fig. 1(b-d). The numerical modeling of the beam-dynamics presented in Fig. 1(b-d), performed with the IMPACT-T [25] program, predicts an ideal mapping of the eigenemittances into projected emittances [see Fig. 1(b)] allowed by the linear space-charge forces supported by the quasi-ellipsoidal distribution [26, 27]. Figure 2(b,c) compares the beam distributions recorded at X1 and X2 and illustrates the transformation of the incoming coupled cylindrical-symmetric beam in the “flat” decoupled beam with a high transverse emittance (and aspect) ratio.

Our experiment employs  $B_c$  as a single knob to control the strength of the transverse coupling  $\mathcal{L}$  to set the initial eigenemittance partition [13]. The photoemitted bunch (with charge  $Q = 1 \pm 0.1$  nC) is accelerated to  $42 \pm 0.5$  MeV before being decoupled by the skew-quadrupole magnets SQ1-3 downstream of the linac. The post-linac beamline includes several diagnostics stations (X1-3). All 3 stations have 50-mm diameter Cerium-doped Yttrium aluminium garnet (Ce:YAG) electron imaging screens to measure the transverse distribution. The slit-scan method is used to measure the phase space. It uses horizontally- and vertically-scanning slits (with respective widths of 100 and 50  $\mu\text{m}$ ) at X2. These slits are scanned across the beam and the transmitted beamlets are recorded at X3 to provide a measurement of the transverse momentum spread associated with the beamlet at the transverse position of the slit. Therefore, the measurement can be used to reconstruct the transverse phase space at X2. In the case of an incoming coupled beam (SQ1-3 turned off) the transmitted beamlets shears, in addition to diverging, as it reach X3. The net shearing angle  $\theta$  provides a measurement of  $\mathcal{L} = \gamma \frac{\sigma_2 \sigma_3 \sin \theta}{D}$ , where  $\sigma_i$  ( $i = 2, 3$ ) stands for the rms beam sizes at  $X_i$ , and  $D$  is the distance separating X2 to X3 [28]. The measured beamlet divergence at X2 associated with the sampled position across the beam at X1 can be used to reconstruct the phase space as illustrated in Fig. 3(a,b) where the  $(y, y')$  phase space of the incoming magnetized beam was measured for two values of magnetization. The phase spaces were reconstructed from 11 sampling positions of the slit and interpolated using linear splines. The  $(x, x')$  phase-space is very similar due to the beam cylindrical symmetry beam and we report only the vertical plane as the smaller-width scanning slit pro-

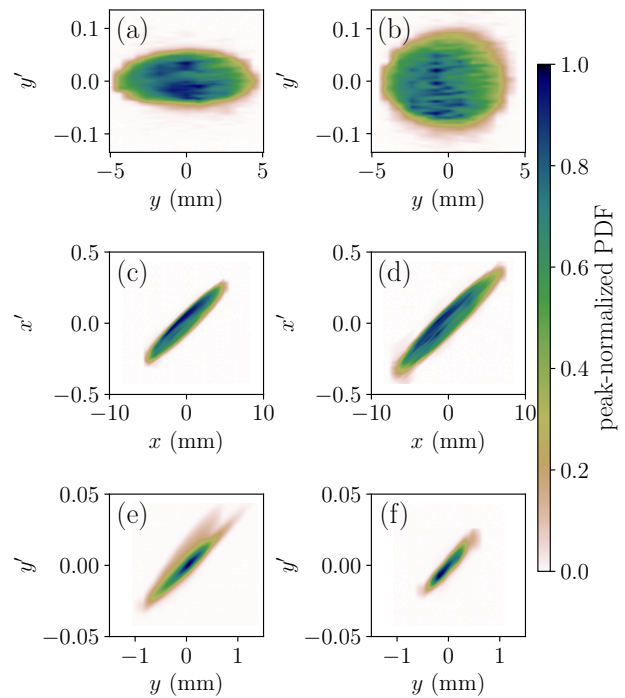


Figure 3. Measured phase-space PDFs of the electron bunch in coupled (a,b) and uncoupled states (c-f) for  $B_c = 79$  mT (a,c,e) and  $B_c = 140$  mT (b,d,f). Plots (a,b):  $(y, y')$  PDF of the round beam; Plots (c,d) and (e,f) are respectively the  $(x, x')$  and  $(y, y')$  PDF of the final uncoupled flat beams.

vides a better resolution than the  $(x, x')$  measurement. The  $(y, y')$  phase-space PDFs shown in Fig. 3(a,b) are uncorrelated, i.e.  $\langle yy' \rangle \simeq 0$ , which is expected as the upstream beamline was tuned to produce a waist close to the slit location for the coupled beam. The emittance directly computed from these “projected” phase-space PDFs yields the projected emittance  $\varepsilon_x$ . Likewise, removing the averaged beamlet shear and analyzing the so-processed beamlets provide a direct measurement of the uncorrelated phase space PDF which provides  $\varepsilon_u$  [29].

The decoupling of the beam dynamics is accomplished with three skew-quadrupole magnets having their strengths set to exert the net torque needed to remove the initial angular momentum. It is generally challenging to diagonalize the beam covariance matrix, and the decoupling transformation  $M$  implemented by the skew-quadrupole magnets produces instead a block-diagonal matrix resulting in the final beam covariance matrix for the uncoupled state,

$$\Sigma_f = M \Sigma \tilde{M} = \begin{bmatrix} \varepsilon_+ T_+ & 0 \\ 0 & \varepsilon_- T_- \end{bmatrix} \text{ with } T_{\pm} = \begin{bmatrix} \beta_{\pm} & -\alpha_{\pm} \\ -\alpha_{\pm} & \gamma_{\pm} \end{bmatrix}$$

where  $\beta_{\pm} > 0$  are the betatron functions,  $\alpha_{\pm} \equiv -\frac{1}{2} \frac{d\beta_{\pm}}{ds}$  measures the phase-space linear correlation and  $\gamma_{\pm} \equiv (1 + \alpha_{\pm}^2)/\beta_{\pm}$  so that  $\det(T_{\pm}) = 1$  and the final projected

emittance associated with  $\Sigma_f$  are  $(\varepsilon_{f,x}, \varepsilon_{f,y}) = (\varepsilon_+, \varepsilon_-)$  (note that the mapping can be swapped by changing the magnets polarity). The pair  $(\alpha_{\pm}, \beta_{\pm})$  is also referred to as the Courant-Snyder (CS) parameters [16]. To devise the skew-quadrupole magnets settings, a beam-

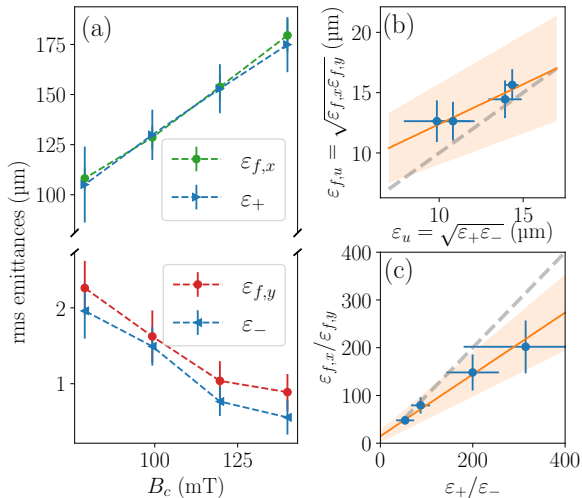


Figure 4. Measurement of eigenemittances associated with the incoming coupled beam  $(\varepsilon_+, \varepsilon_-)$  and the final projected emittances  $(\varepsilon_x, \varepsilon_y)$  after decoupling for different values of the magnetic field on the photocathode surface  $B_c$  (a). Transfer of the uncorrelated emittances (b) and emittance ratio (c). The identity line is shown as a grey-dash line in (b) and (c) and the orange line with shaded area respectively correspond to a linear regression with associated  $1\sigma$  confidence interval.

envelope fitting technique [30], using the screens X1-3, was used to obtain the CS parameters at the entrance of the skew-quadrupole channel. These CS parameters were then used as inputs to optimize the skew settings to decouple the motion. The optimization was performed with IMPACT-T simulation considering the realistic quadrupole-magnet field profiles and taking into account space-charge effects. These settings of the skew strengths were further experimentally fine-tuned to ensure the beam remained “flat” when observed on X2 and X3 – thereby experimentally confirming the coupling is fully canceled. Finally, slit-scan measurements were conducted to measure the horizontal and vertical phase space PDFs associated with the flat beam. Our choice to produce a vertically-flat beam stems from the higher-resolution diagnostics available for the vertical phase space. Figure 3(c-f) displays such PDF for two cases of initial coupling. For large values of  $\mathcal{L}$  the reconstructed phase spaces are highly unbalanced [the phase-space area of the  $(x, x')$  is up to  $\sim 200$  times larger than  $(y, y')$ ]; see Figure 3(d,f). The asymmetry between the two final transverse phase spaces can be observed by examining Fig. 3(c,d) and (e,f).

From the measured coupling  $\mathcal{L}$  and uncorrelated

emittance  $\varepsilon_u$ , eigenemittances of the coupled beam are calculated from Eq. 2 with  $\xi_{\pm} = 2(\varepsilon_{\perp}^2 + \mathcal{L}^2 \pm \varepsilon_{4d})$  for a round beam and defining  $\varepsilon_{\perp} \equiv [\varepsilon_u^2 + \mathcal{L}^2]^{1/2}$ , with  $\varepsilon_u \equiv \varepsilon_{4d}^{1/2}$ , we obtain [21]  $\varepsilon_{\pm} = [\varepsilon_u^2 + \mathcal{L}^2]^{1/2} \pm \mathcal{L}$ . The measured eigenemittances are compared with the final projected emittances after the decoupling transformation  $(\varepsilon_{f,x}, \varepsilon_{f,y})$  in Fig. 4(a). We generally find an excellent agreement for the mapping  $\varepsilon_+ \mapsto \varepsilon_{f,x}$  and  $\varepsilon_- \mapsto \varepsilon_{f,y}$ . Figure 4(b) displays the evolution of the  $\varepsilon_u$  obtained from the coupled  $(\varepsilon_u = \sqrt{\varepsilon_- \varepsilon_+})$  and decoupled states  $\varepsilon_{f,u} = \sqrt{\varepsilon_{f,x} \varepsilon_{f,y}}$ . We note that the value of  $\varepsilon_u$  differs for each case of  $B_c$  as our experimental configuration does not provide an independent control over the cross-plane correlation imposed on the beam and the emittance-compensation process which minimizes the value of  $\varepsilon_u$  [31–34]. Nevertheless the measured  $\varepsilon_{u,f}$  and  $\varepsilon_u$  agrees within  $\lesssim 20\%$  relative error. Finally Fig. 4(d) shows that unprecedented transverse emittance ratios  $\varepsilon_{f,x}/\varepsilon_{f,y} \gtrsim 200$  – were attained in our experiment. The mapping is near ideal with some discrepancies observed for high values of  $B_c$  due to the limited resolution of our diagnostics to resolve the small values of  $\varepsilon_{f,y}$ .

In summary, we have experimentally demonstrated the transfer of generalized kinematical invariants – the eigenemittances – associated with a coupled beam to invariants associated with the lower-dimension orthogonal degrees of freedom after decoupling the beam via a linear transformation. These results confirm the potential of these generalized invariants to precisely control the phase-space partition between the degrees of freedom via tailoring of initial cross-plane correlations. Our findings could be generalized to configurations with higher dimensionality (e.g. introducing coupling between all DOFs) as proposed in [8]. Our research could also have applications to Optics and Quantum Mechanics where similar invariants are often introduced to describe coupled-motion or mixed-states configurations.

This work was supported by the U.S. Department of Energy (DOE), Office of Science, under award No. DE-SC0018656 with Northern Illinois University and contract No. DEAC02-06CH11357 with Argonne National Laboratory (ANL). We also acknowledge support from the “US-DOE-Japan cooperation in High-Energy Physics” program and computing resources provided on BEBOP, a high-performance computing cluster operated by the Laboratory Computing Resource Center at ANL.

\* xu@niu.edu

[1] A. J. Dragt, F. Neri, and G. Rangarajan, General moment invariants for linear hamiltonian systems, *Phys. Rev. A* **45**, 2572 (1992).

- [2] S. D. Bartlett, T. Rudolph, and R. W. Spekkens, Reconstruction of gaussian quantum mechanics from Liouville mechanics with an epistemic restriction, *Phys. Rev. A* **86**, 012103 (2012).
- [3] R. Simon and N. Mukunda, Optical phase space, wigner representation, and invariant quality parameters, *J. Opt. Soc. Am. A* **17**, 2440 (2000).
- [4] F. Neri and G. Rangarajan, Kinematic moment invariants for linear hamiltonian systems, *Phys. Rev. Lett.* **64**, 1073 (1990).
- [5] J. Liouville, Note sur la théorie de la variation des constantes arbitraires, *Journal de Mathématiques Pures et Appliquées* **3**, 342 (1838).
- [6] P. M. Lapostolle, Possible emittance increase through filamentation due to space charge in continuous beams, *IEEE Transactions on Nuclear Science* **18**, 1101 (1971).
- [7] V. V. Dodonov and O. V. Man'ko, Universal invariants of quantum-mechanical and optical systems, *J. Opt. Soc. Am. A* **17**, 2403 (2000).
- [8] L. D. Duffy and A. J. Dragt, Chapter one - utilizing the eigen-emittance concept for bright electron beams, in *Advances in Imaging and Electron Physics*, Vol. 193, edited by P. W. Hawkes (Elsevier, 2016) pp. 1–44.
- [9] R. Brinkmann, Y. Derbenev, and K. Flöttmann, A low emittance, flat-beam electron source for linear colliders, *Phys. Rev. ST Accel. Beams* **4**, 053501 (2001).
- [10] M. Cornacchia and P. Emma, Transverse to longitudinal emittance exchange, *Phys. Rev. ST Accel. Beams* **5**, 084001 (2002).
- [11] N. Yampolsky, B. Carlsten, R. Ryne, K. Bishofberger, S. Russell, and A. Dragt, *Controlling electron-beam emittance partitioning for future x-ray light sources* (2010), arXiv:1010.1558 [physics.acc-ph].
- [12] P. Piot, Y.-E. Sun, and K.-J. Kim, Photoinjector generation of a flat electron beam with transverse emittance ratio of 100, *Phys. Rev. ST Accel. Beams* **9**, 031001 (2006).
- [13] L. Gröning, M. Maier, C. Xiao, L. Dahl, P. Gerhard, O. K. Kester, S. Mickat, H. Vormann, M. Vossberg, and M. Chung, Experimental proof of adjustable single-knob ion beam emittance partitioning, *Phys. Rev. Lett.* **113**, 264802 (2014).
- [14] G. Ha, K. J. Kim, P. Piot, J. G. Power, and Y. Sun, *Bunch shaping in electron linear accelerators* (2021), arXiv:2111.00520 [physics.acc-ph].
- [15] J. Williamson, On the algebraic problem concerning the normal forms of linear dynamical systems, *American Journal of Mathematics* **58**, 141 (1936).
- [16] E. Courant and H. Snyder, Theory of the alternating-gradient synchrotron, *Annals of Physics* **3**, 1 (1958).
- [17] L. Gröning, C. Xiao, and M. Chung, Particle beam eigen-emittances, phase integral, vorticity, and rotations, *Phys. Rev. Accel. Beams* **24**, 054201 (2021).
- [18] B. E. Carlsten, K. A. Bishofberger, L. D. Duffy, S. J. Russell, R. D. Ryne, N. A. Yampolsky, and A. J. Dragt, Arbitrary emittance partitioning between any two dimensions for electron beams, *Phys. Rev. ST Accel. Beams* **14**, 050706 (2011).
- [19] M. E. Conde, D. S. Doran, W. Gai, R. Konecny, W. Liu, J. G. Power, Z. M. Yusof, S. P. Antipov, C. J. Jing, and E. E. Wisniewski, Upgrade of the Argonne Wakefield Accelerator Facility (AWA): Commissioning of the RF Gun and Linac Structures for Drive Beam Generation, *Conf. Proc. C* **110904**, 2799 (2011).
- [20] A. Burov, S. Nagaitsev, and Y. Derbenev, Circular modes, beam adapters, and their applications in beam optics, *Phys. Rev. E* **66**, 016503 (2002).
- [21] K.-J. Kim, Round-to-flat transformation of angular-momentum-dominated beams, *Phys. Rev. ST Accel. Beams* **6**, 104002 (2003).
- [22] A. Halavanau, G. Qiang, G. Ha, E. Wisniewski, P. Piot, J. G. Power, and W. Gai, Spatial control of photoemitted electron beams using a microlens-array transverse-shaping technique, *Phys. Rev. Accel. Beams* **20**, 103404 (2017).
- [23] O. J. Luiten, S. B. van der Geer, M. J. de Loos, F. B. Kiewiet, and M. J. van der Wiel, How to realize uniform three-dimensional ellipsoidal electron bunches, *Phys. Rev. Lett.* **93**, 094802 (2004).
- [24] P. Musumeci, J. T. Moody, R. J. England, J. B. Rosenzweig, and T. Tran, Experimental generation and characterization of uniformly filled ellipsoidal electron-beam distributions, *Phys. Rev. Lett.* **100**, 244801 (2008).
- [25] J. Qiang, S. Lidia, R. D. Ryne, and C. Limborg-Deprey, Three-dimensional quasistatic model for high brightness beam dynamics simulation, *Phys. Rev. ST Accel. Beams* **9**, 044204 (2006).
- [26] I. M. Kapchinskij and V. V. Vladimirkij, Limitations Of Proton Beam Current In A Strong Focusing Linear Accelerator Associated With The Beam Space Charge, in *2nd International Conference on High-Energy Accelerators* (1959) pp. 274–287.
- [27] P. M. Lapostolle, *Effets de la charge d'espace dans un accélérateur linéaire à protons*, Tech. Rep. CERN-AR-Int-SG-65-15 (CERN, Geneva, 1965).
- [28] Y. Sun, P. Piot, K.-J. Kim, N. Barov, S. Lidia, J. Santucci, R. Tikhoplav, and J. Wennerberg, Generation of angular-momentum-dominated electron beams from a photoinjector, *Phys. Rev. ST Accel. Beams* **7**, 123501 (2004).
- [29] F. Hannon and M. Stefani, Transverse uncorrelated emittance diagnostic for magnetized electron beams, *Phys. Rev. Accel. Beams* **22**, 102801 (2019).
- [30] K. McDonald and D. Russell, Methods of emittance measurement, in *Frontiers of Particle Beams; Observation, Diagnosis and Correction. Lecture Notes in Physics*, Vol. 343, edited by M. Month and S. Turner (Springer, Berlin, Heidelberg, 1989).
- [31] B. Carlsten, New photoelectric injector design for the los alamos national laboratory XUV FEL accelerator, *Nuclear Instruments and Methods in Physics Research Section A: Accelerators, Spectrometers, Detectors and Associated Equipment* **285**, 313 (1989).
- [32] L. Serafini and J. B. Rosenzweig, Envelope analysis of intense relativistic quasilaminar beams in rf photoinjectors: a theory of emittance compensation, *Phys. Rev. E* **55**, 7565 (1997).
- [33] X. Chang, I. Ben-Zvi, and J. Kewisch, Compensation for bunch emittance in a magnetization and space charge dominated beam, *AIP Conference Proceedings* **737**, 462 (2004), <https://aip.scitation.org/doi/pdf/10.1063/1.1842578>.
- [34] S. Miginsky, Emittance compensation of elliptical beams, *Nuclear Instruments and Methods in Physics Research Section A: Accelerators, Spectrometers, Detectors and Associated Equipment* **603**, 32 (2009), proceedings of the XVII International Synchrotron Radiation Conference.